Observation of short-range Yu-Shiba-Rusinov states with threefold symmetry in layered superconductor 2H-$NbSe_2$

Xing Yang[1], Yuan Yuan[1], Yang Peng[2,3], Emi Minamitani[4], Lang Peng[1], Jing-Jing Xian[1], Wen-Hao Zhang[1], Ying-Shuang Fu[1*]

1. School of Physics and Wuhan National High Magnetic Field Center, Huazhong University of Science and Technology, Wuhan 430074, China
2. Department of Physics and Astronomy, California State University, Northridge, Northridge, California, 91330, USA
3. Institute of Quantum Information and Matter and Department of Physics, California Institute of Technology, California, 91125, USA
4. Institute for Molecular Science, Okazaki 444-8585, Japan

Email: * yfu@hust.edu.cn

Yu-Shiba-Rusinov (YSR) state arises when magnetic impurities interact with hosting superconductivity. The intricacy of coupling and the nature of the superconductivity determine the behavior of the YSR state, whose detailed correlations are not yet fully understood. Here we study the YSR state of single Fe adatom on the surface of 2H-$NbSe_2$ with combined low temperature scanning tunneling microscopy/spectroscopy, density functional theory calculations and tight-binding modeling. It is found that the Fe adatom occupies the hollow site of the Se surface layer. Prominent YSR state close to the Fermi level is observed. The YSR state exhibits threefold symmetry along the diagonal direction of the Se lattice. The spatial decay of the YSR state follows a behavior in three-dimensional superconductivity. This behavior contrasts with a previous study of imbedded Fe impurities, whose YSR state shows six-fold symmetry and two-

dimensional long-range decay [Ref. 23]. According to our theoretical modeling, the coupling configurations affect the adatom-substrate hopping and the interlayer coupling of the substrate. Both factors are crucial for the consequent behavior of the YSR state.

The local magnetic moment of magnetic impurities on surfaces of superconductors leads to a pair breaking effect in superconductivity and forms low-energy bound states inside the superconductor gap, which are named as YSR states [1-3]. The YSR bound states appear in pairs that are particle-hole symmetric relative to Fermi level, whose energy is determined by the spin of the local magnetic moment and its exchange coupling strength with the superconducting electrons [4, 5]. Since their first observation at single Gd and Mn impurities on Nb surface with scanning tunneling microscopy [6], fruitful properties of YSR states are revealed. These studies include the identification of spin polarization [7], and multiple YSR peaks from different angular momenta [8], magnetic anisotropy [9] and orbital structure of the local magnetic moment [10, 11]. Moreover, the YSR state has been utilized as a probe to study the exchange interaction between magnetic impurities [12, 13] and the competition between Kondo screening and pair breaking effect in superconductivity [14].

The interplay between the coupling of YSR states and spin-orbit coupling provides a platform for realizing topological superconductivity, which features Majorana modes at the boundary [15-22]. Due to the localized nature of YSR states, their mutual coupling requires a short separation between the magnetic impurities, which are typically on the atomic scale. Recently, Ménard *et al*. found long-range YSR states with a decay length of ~10 nm

expressing sixfold symmetry on Fe impurities imbedded in layered superconductor 2H-$NbSe_2$, which are interpreted as a courtesy of the two-dimensional property of superconductivity [23]. This compelling observation renders the possibility of constructing topological superconductor through long-range YSR state. However, the Fe impurities in the study were introduced unintentionally and the coupling between the YSR states are not controllable with atom manipulation based on STM because they are imbedded in the crystal.

In this regard, we deposited Fe adatoms on the surface of $NbSe_2$ substrate with molecular beam epitaxy in ultrahigh vacuum condition at low temperature and characterized their YSR states with scanning tunneling microscopy (STM) and spectroscopy (STS). The Fe adatoms provide well-defined magnetic impurities and are readily manipulated with the tip of STM. In contrast to previous observation, the YSR states surprisingly exhibit short-range decay and threefold symmetry. Our theoretical modeling suggests that the threefold symmetry is related to the occupation site of Fe adatom on $NbSe_2$. Our work reveals the importance of adsorption geometry on the behavior of YSR states, paving the way of further studying coupled YSR states on layered superconductors.

Our experiment was carried out in a custom-designed Unisoku STM (1300) at ~0.4 K [24]. Single crystals of 2H-$NbSe_2$ were cleaved in situ under ultra-high vacuum conditions at ~77 K. After cleaving, Fe atoms (Alfa Aesar, purity 99.998%) were evaporated onto the pristine surface at low temperature of ~30 K to get isolated Fe adatoms. Next, the sample was transferred quickly into STM chamber for subsequent measurements. An electro-etched

W tip is used for the STM probing, which has been cleaned and characterized on a Ag(111) substrate prior to the measurement. The tunneling spectra were recorded by standard lock-in technique with a modulation voltage (V_{mod}) of 50 μV at a frequency of 983 Hz. Our density functional theory (DFT) calculations were performed with Vienna An-initio Simulation Package (VASP) [25,26] with the projected augmented wave method [27]. The GGA-PBE exchange correlation functional was used in all calculations. The kinetic energy cut-offs of the plane wave basis were set to 400 eV. The impurity configuration was modeled by 4×4 supercell of single layer $NbSe_2$ with a single Fe adatom at on-top site of Nb, on-top site of Se, or hollow site. The coordinates of Fe and atoms in $NbSe_2$ monolayer were optimized without any constraint until the forces acting on individual atoms becomes less than 20 meV/Å.

Fig. 1(a) shows the topography of four single Fe adatoms on $NbSe_2$ surface. On the $NbSe_2$ substrate, there is a CDW pattern with a periodicity of about 3 times the lattice constant of top Se layer. The Fe adatoms appear as bright protrusions with an apparent height of 96 pm and a size of 0.76 nm. From the high resolution STM image, the adsorption site of the Fe adatoms are determined as the hollow-site of the top Se atom layer [Fig. 1(a), inset]. In addition, the shape of the Fe adatom exhibits bias dependence. It is round-shaped at an imaging bias of 100 meV and becomes triangular-shaped at the low imaging bias of 20 meV [Figs. 1(b) and (c)].

Our DFT simulations also identifies the most energetically favorable adsorption site is the hollow site, which is 0.424 eV/atom and 2.481 eV/atom smaller in energy compared to

the adsorption on the on-top site of Nb and the on-top site of Se is, respectively. The adsorption results electron charge transferring from Fe predominantly to the nearest Nb atoms [Fig. 1(d)]. From our DFT calculations, spin polarizations of the five *d* orbitals of the Fe adatom are all survived upon the adsorption on $NbSe_2$, resulting a magnetic moment of 3.784 μ_B. The spin polarization is mainly on Fe atom, but the nearest Nb atoms also get slightly spin-polarized [Fig. 1(e)].

Next, we study the effect of local magnetic moment from the Fe adatom on superconductivity. Fig.2(a) shows a STM image of a typical Fe adatom. The d*I*/d*V* spectra were taken at the edge of the Fe adatom exhibit a prominent YSR bound state inside the superconducting gap, whose energy is close to the zero bias, demonstrating its strong pair breaking effect [Fig. 2(b)]. The shape of the bound state appears asymmetric. It is a consequence of overlap from the particle and hole parts of the YSR states, which have different intensity. In addition to the asymmetric bound state near zero bias, the occupied coherence peak has higher intensity than its unoccupied counterpart. This suggests the existence of another pair of YSR bound states that are close to the coherence peaks. Surprisingly, the YSR states are barely seen at the center of the Fe adatom. There is minute density of states inside the superconducting gap and similar asymmetric conductance intensity at the coherence peaks. This indicates the YSR states are not evenly distributed on the Fe atom, whose spatial evolution calls for a spectroscopic imaging to the YSR state.

We then focus on the YSR state close to the Fermi level. The spectroscopic mapping is obtained by setting at 0.15 mV, corresponding to the energy of the YSR state that has the

highest intensity. As shown in Fig.2(c), spatial distribution of the YSR state displays a three-fold symmetric pattern. It is indeed suppressed at the atomic center and enhanced at edges of the Fe atom along three symmetry axes of the Se lattice. The conductance intensity of the YSR state becomes significantly smaller and eventually unresolvable upon further increasing distance from the Fe center. This contrasts with previous studies on imbedded Fe impurities in 2H-$NbSe_2$, where a six-fold symmetric star-shaped pattern is observed, and the star center has strongest intensity [23]. It is also note that the spectral intensity of the YSR states at the edge of the Fe adatom in our case is stronger than that at the center of the imbedded Fe atom in the previous study [23]. Presumably, the Fe adatom is closer to the STM tip and has increased contribution to the tunneling signal.

Having identified the spatial distribution symmetry of the YSR state, we further study its spatial extension quantitatively to examine its decay behavior. Fig.2(d) is a 2D conductance plot taken across the Fe adatom along the red dotted line in Fig. 2(a). Note that the zero position is set at the center of the Fe atom. In addition to the strongest YSR state intensity at the edge of the Fe atom, the second strongest YSR intensity appear at ~1.4 nm from the Fe center. With further increasing distance, the YSR intensity rapidly decreases and becomes barely seen after the second oscillation. This observation is in consistency with the spectroscopic mapping. For YSR states, its decay behavior in real space follows an oscillatory manner, whose periodicity is related to the Fermi vector k_F. The relation between the distance *r* and the local density of states of the YSR state $|\psi_{\pm}|^2$ can be written as

$$|\psi_{\pm}|^2 \propto (sin(k_F r + a))^2 / r^{D-1} \cdot exp(-r/b)$$

Here, a and b are two constants determined by the specific scattering potential from the magnetic impurity. The lower index in $|\psi_{\pm}|^2$ represents the particle and hole component of the YSR wave function. D depicts dimensionality of the superconductor, where $D = 2$ for 2D case and $D = 3$ for 3D case, respectively. To quantitatively evaluate the decay behavior, we extracted a line cut along the green line in Fig. 2(d). Subsequently, we performed numerical simulations with the decay rate of 2D and 3D superconductivity, respectively [Fig. 2(e)]. Obviously, simulation of the 3D case delivers a significantly better fitting compared to that of 2D. The fitting gives a k_F of ~0.32 Å^{-1}, which agrees with previous report (Ref. [23]). However, the spatial decay showing $b = 2.8$ nm is in distinct contrast to that of the imbedded Fe impurity, which has a 2D decay behavior.

We have also evaluated the influence of CDW pattern on the YSR state. Figure 3(a) shows four Fe adatoms which are located at different positions relative to the CDW pattern. The spatial distribution of the YSR states for the four Fe adatoms overall express threefold symmetry [Fig. 3(b)]. And, the CDW pattern merely contributes corrections to the symmetry by making one arm of the YSR states darker in atom 4 and brighter in atom 2. Similar behavior of symmetry correction is observed in the imbedded Fe atoms [23], presumably due to the CDW as well. Moreover, there is no obvious difference on the spatial extension of the YSR states of the four atoms. For all the measured atoms whose number is approximately 30, we didn't observe any atoms whose YSR states deviate dramatically from the threefold symmetry and the short-range decay behavior. Therefore, the leading features of the YSR

state are not affected by the CDW pattern. We notice a systematic study on the correlation between the CDW pattern and the YSR states has been reported very recently [28].

Energy of the YSR states are governed by the Kondo like exchange coupling *J* between the magnetic impurities and Cooper pairs in the superconductor. The *J* is directly related to the hybridization strength of the impurity and substrate, which is governed by the local crystal field of the absorption site [10]. In addition to its energy, the J, in conjunction with the anisotropy of the Fermi surface of the substrate [29], also determines the spatial anisotropy of the YSR state. $NbSe_2$ possess valley characteristic Fermi surfaces, rendering it an ideal substrate for addressing the effect of *J* on the spatial symmetry of the YSR state. YSR states on $NbSe_2$ have been investigated in several studies with spectroscopic measurements of STM [28,30,31]. When the Fe is absorbed on the hollow site of three Nb atoms, a threefold symmetry YSR should be expected. This is indeed confirmed based on a tight-binding calculation. Particularly, we take the same 1-band model characterizing the lowest-lying Nb 4d-derived states of 2H-$NbSe_2$ [23]. Instead of introducing a hopping amplitude between the adatom orbital and a single triangular site as done in Ref. [23], which gives rise to a sixfold YSR state [Fig. 4(a)], we model the threefold absorption site by introducing a finite hopping amplitude between the adatom orbital and the three nearest neighbor triangular sites, which leads to a threefold YSR state [Fig. 4(b)].

For the short-range decay of the YSR state, we provide an analytical argument. Given the fact that the spatial decay of the YSR state is closely related to the spatial profile of real space electron Green function, or propagator, of the superconducting substrate (see Ref. [23]

for details), we compute this quantity for a system consisting layers of 2D BCS superconductors. In the supplemental material, we show that in the asymptotic limit $k_F r \gg 1$, where k_F is the Fermi momentum and r is the real space coordinate within the layer, the YSR state wave function at first decays as $1/\sqrt{r}$ (2D decay) and then changes into a $1/r$-form of decay at larger distance, with a crossover distance $r_c \sim v_F/(2t)$, where v_F is the Fermi velocity of a single layer 2H-$NbSe_2$, and t is the interlayer coupling strength of 2H-$NbSe_2$. This leads to a plausible explanation for the discrepancies between the long-range decay of the YSR state observed in Ref. [23] and the short-range decay observed in ours. In the former case, the magnetic impurities are imbedded in the 2H-$NbSe_2$, which may strongly distort the lattice locally and thus reduce the interlayer coupling near these impurities. In the latter case, on the other hand, the adatoms are all adsorbed on a single layer, the layered structure gets less distorted and thus we can expect a larger interlayer coupling t. Hence, it can be expected that our system has a smaller r_c, which makes the YSR states decay much faster.

Before concluding, we note that the electron and hole components of the YSR states are split in energy in Ref. 23, but overlap in our case. Our study indicates that such overlapping doesn't affect the symmetry and decay behavior. Our modeling reveals the symmetry of the YSR state is dominated by the exchange coupling to the local environment. The adsorbed Fe atom has a threefold environment, endowing its YSR state with threefold symmetry for both the electron and hole components. On the other hand, the decay of the YSR state is related

to the dimensionality of the hosting superconductivity, which is irrelevant to the overlap of electron and hole like YSR states either.

In conclusion, we have investigated the YSR states of single Fe adatom on layered superconductor 2H-$NbSe_2$. The spatial distribution of the YSR states exhibits a characteristic pattern with threefold symmetry. It is ascribed as the result of the specific hollow-site adsorption configuration of Fe adatom on $NbSe_2$ surface. The YSR state has short-range spatial extension conforming to a decay behavior of 3D superconductivity. This implies that the inter-layer interaction of 2H-$NbSe_2$ has substantial influence on the local environment of adsorbed Fe adatom. Our results may provide help for clarifying the dimensional dependence of YSR states in layered superconductors.

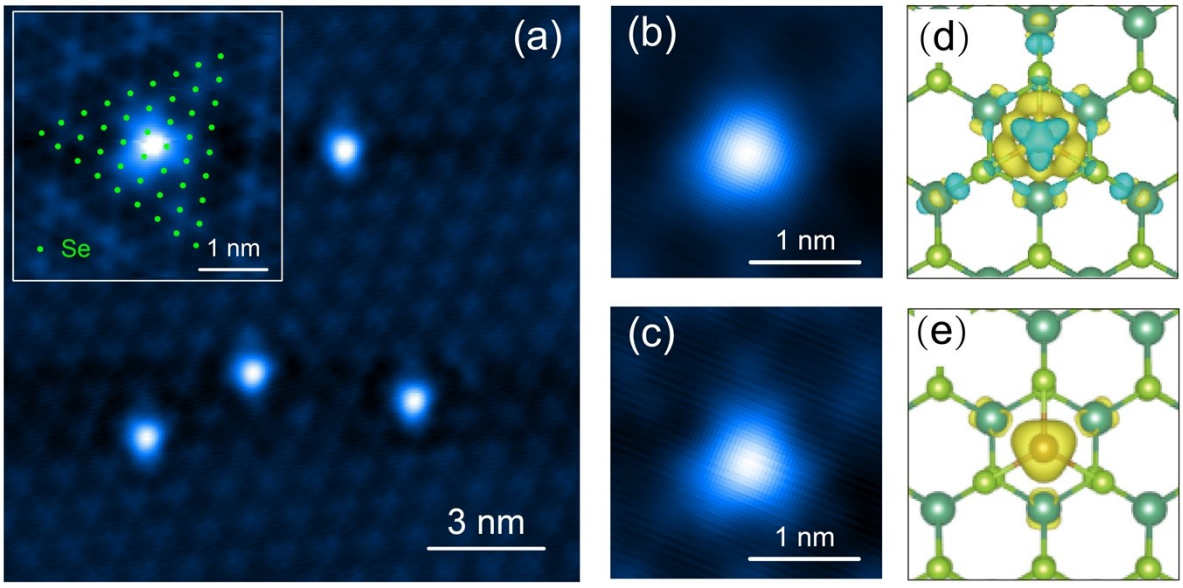

Figure 1. Topography of Fe adatom on $NbSe_2$. (a) STM image (V_t = -500 mV, I_t = 100 pA) of Fe adatoms deposited on $NbSe_2$ surface. The inset is a zoom in image (V_t = 8 mV, I_t = 20 pA) of a single Fe atom superimposed with atomic positions of Se lattices. (b, c) Bias dependent topography of single Fe adatom. Imaging conditions: V_t = 100 mV, I_t = 100 pA for (b), and V_t = 20 mV, I_t = 100 pA for (c). (d) DFT calculated charge redistribution around the Fe adatom, which is adsorbed at hollow site of the Se lattice. The cyan and yellow colors represent depletion and accumulation of electrons. The light (dark) green balls depict Se (Nb) atoms. (e) DFT calculated spin distribution of Fe adatom (orange ball), which is represented with yellow color.

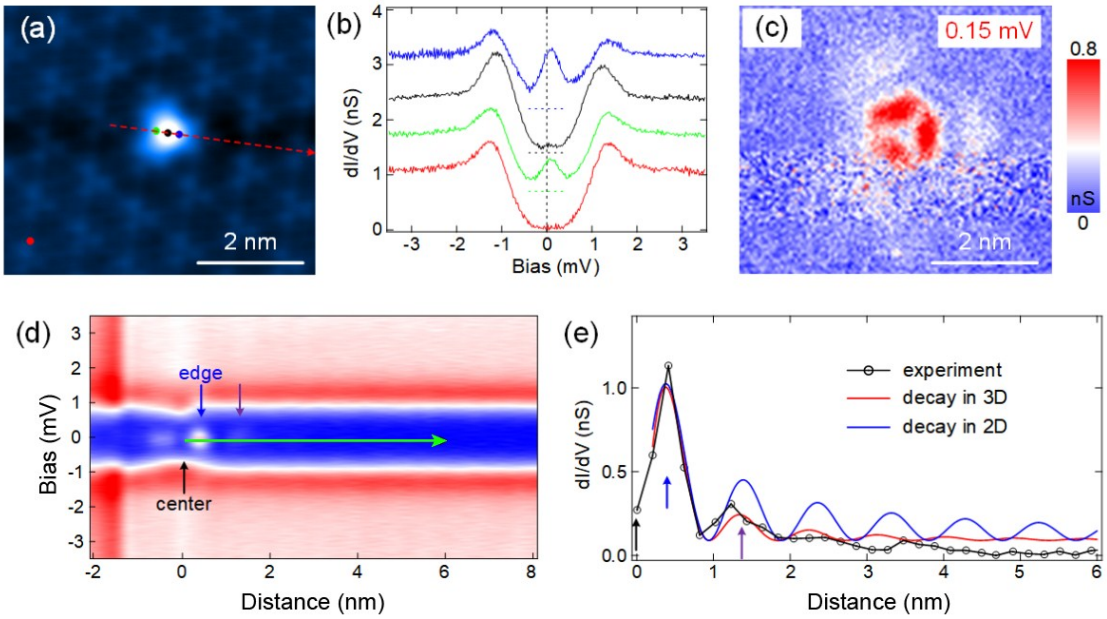

Figure 2. YSR state of single Fe atom. (a) Topography of single Fe adatom. Imaging condition: V_t = 80 mV, I_t = 20 pA. (b) dI/dV spectra taken at different locations of the Fe adatom. The spectra have been shifted vertically for clarity and the zero conductance for each spectrum is indicated by horizontal dashed lines. Spectroscopic set point: V_t = 4 mV, I_t = 100 pA. (c) dI/dV mapping of the YSR state of single Fe adatom taken at 0.15 mV. Spectroscopic set point: V_t = 3 mV, I_t = 80 pA. (d) 2D conductance plot taken along the red dashed line in (a), showing the spatial evolution of the YSR states. Spectroscopic set point: V_t = 4 mV, I_t = 100 pA. (e) Conductance line profile (black dotted line) extracted along the green line in (d). The numerically simulated curves, showing the spatial decay of the YSR states based on 3D and 2D superconductivity, are marked in red and blue lines, respectively.

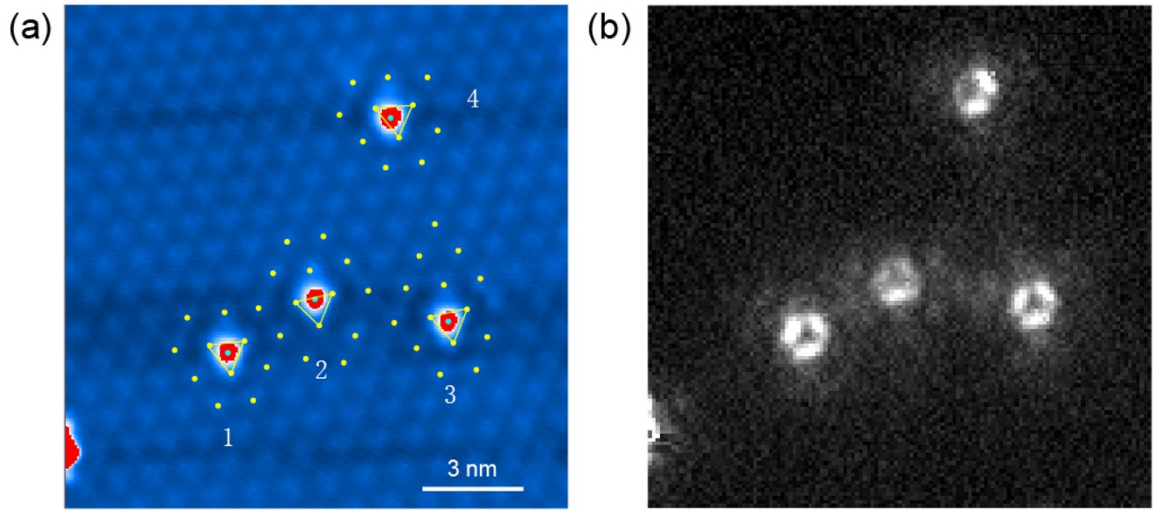

Figure 3. Influence of CDW on the YSR state. (a) STM image of Fig. 1(a) whose color scale is adjusted to enhance the CDW pattern. The centers of the Fe adatoms and CDW patterns are marked with green and yellow dots, respectively. The red (blue) color represents high (low). (b) The dI/dV mapping of the identical area in (a), showing the spatial distribution of the YSR states. (Spectroscopic parameters: V_t = -2 mV, I_t = 50 pA, V_{mod} = 0.05 mV).

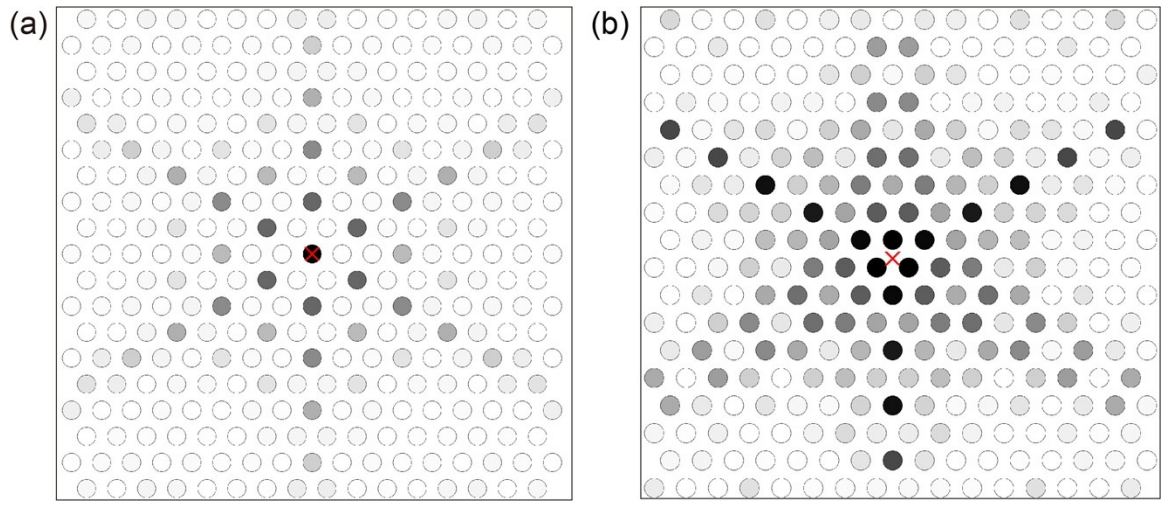

Figure 4. Tight-binding modeling of YSR states. (a) Spatial distribution pattern of $|\psi_-|^2$ for YSR states (grey solid dot) from on-top Fe adatom, showing sixfold symmetry. (b) Spatial distribution pattern of $|\psi_-|^2$ for YSR states (grey solid dot) from hollow site Fe adatom, showing threefold symmetry. In (a) and (b), the open dots and a red cross depict Nb atoms and the Fe adatom, respectively. Higher intensity of the YSR states corresponds to darker grey color. See supplemental material for detailed description of the tight-binding calculation.

Acknowledgement:

This work is funded by the National Key Research and Development Program of China (Grant No. 2017YFA0403501, 2016YFA0401003, 2018YFA0307000), the National Science Foundation of China (Grants No. 11874161, No. 11522431, No. 11474112). Y.P.

acknowledges support from the startup fund from California State University, Northridge, as well as support from the IQIM, an NSF physics frontier center funded in part by the Moore Foundation at Caltech.

References:

1. L. Yu. Acta Physica Sinica, 21(1), 75 (1965).
2. H. Shiba. Progress of Theoretical Physics, 40(3), 435 (1968).
3. A.I. Rusinov. Sov. Phys. JETP, 29(6), 1101 (1969).
4. M.E. Flatté and J.M. Byers. Physical Review Letters, 78(19), 3761 (1997).
5. A.V. Balatsky, I. Vekhter and J.-X. Zhu. Reviews of Modern Physics, 78(2), 373 (2006).
6. A. Yazdani, B.A. Jones, C.P. Lutz, M.F. Crommie and D.M. Eigler. Science, 275(5307), 1767 (1997).
7. L. Cornils, A. Kamlapure, L. Zhou, S. Pradhan, A.A. Khajetoorians, J. Fransson, J. Wiebe and R. Wiesendanger. Physical Review Letters, 119(19), 197002 (2017).

8. S.-H. Ji, T. Zhang, Y.-S. Fu, X. Chen, X.-C. Ma, J. Li, W.-H. Duan, J.-F. Jia and Q.-K. Xue. Physical Review Letters, 100(22), 226801 (2008).

9. N. Hatter, B.W. Heinrich, M. Ruby, J.I. Pascual and K.J. Franke. Nature Communications, 6(1), 8988 (2015).

10. M. Ruby, Y. Peng, F. von Oppen, B.W. Heinrich and K.J. Franke. Physical Review Letters, 117(18), 186801 (2016).

11. D.-J. Choi, C. Rubio-Verdú, J. de Bruijckere, M.M. Ugeda, N. Lorente and J.I. Pascual. Nature Communications, 8(1), 15175 (2017).

12. S. Kezilebieke, M. Dvorak, T. Ojanen and P. Liljeroth. Nano Letters, 18(4), 2311 (2018).

13. D.-J. Choi, C.G. Fernández, E. Herrera, C. Rubio-Verdú, M.M. Ugeda, I. Guillamón, H. Suderow, J.I. Pascual and N. Lorente. Physical Review Letters, 120(16), 167001 (2018).

14. K.J. Franke, G. Schulze and J.I. Pascual. Science, 332(6032), 940 (2011).

15. S. Nadj-Perge, I.K. Drozdov, B.A. Bernevig and A. Yazdani. Physical Review B, 88(2), 020407 (2013).

16. J. Klinovaja, P. Stano, A. Yazdani and D. Loss. Physical Review Letters, 111(18), 186805 (2013).

17. M.M. Vazifeh and M. Franz. Physical Review Letters, 111(20), 206802 (2013).

18. S. Nadj-Perge, I.K. Drozdov, J. Li, H. Chen, S. Jeon, J. Seo, A.H. MacDonald, B.A. Bernevig and A. Yazdani. Science, 346(6209), 602 (2014).

19. M. Ruby, F. Pientka, Y. Peng, F. von Oppen, B.W. Heinrich and K.J. Franke. Physical Review Letters, 115(19), 197204 (2015).

20. B. Braunecker and P. Simon. Physical Review Letters, 111(14), 147202 (2013).

21. F. Pientka, L.I. Glazman and F. von Oppen. Physical Review B, 88(15), 155420 (2013).

22. Y. Kim, M. Cheng, B. Bauer, R.M. Lutchyn and S. Das Sarma. Physical Review B, 90(6), 060401 (2014).

23. G.C. Ménard, S. Guissart, C. Brun, S. Pons, V.S. Stolyarov, F. Debontridder, M.V. Leclerc, E. Janod, L. Cario, D. Roditchev, P. Simon and T. Cren. Nature Physics, 11(12), 1013 (2015).

24. L. Peng *et al*., Nature Communications 8, 659 (2017).

25. G. Kresse and J. Furthmüller, Phys. Rev. B 54, 11169 (1996).

26. G. Kresse and J. Furthmüller, Computational Materials Science 6, 15 (1996).

27. P. E. Blöchl, Phys. Rev. B 50, 17953 (1994).

28. E. Liebhaber *et al*., Nano Lett. 20, 339-344 (2020).

29. M. I. Salkola, A. V. Balatsky, and J. R. Schrieffer, Phys. Rev. B 55, 12648 (1997).

30. S. Kezilebieke, R. Žitko, M. Dvorak, T. Ojanen, P. Liljeroth. Nano Lett. 19, 4614-4619 (2019).

31. S. Kezilebieke, M. Dvorak, T. Ojanen, and P. Liljeroth. Nano Lett. 18, 2311-2315 (2018).